

Panoply of Ni-Doping-Induced Reconstructions, Electronic Phases, and Ferroelectricity in **1T-MoS₂**

Rijan Karkee and David A. Strubbe*

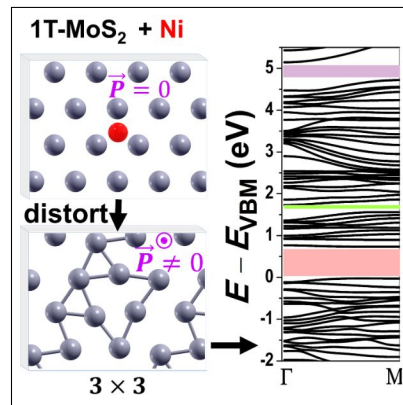
Department of Physics, University of California, Merced, CA 95343

E-mail: dstrubbe@ucmerced.edu

Abstract

The distorted phases of monolayer 1T-MoS₂ have distinct electronic properties, with potential applications in optoelectronics, catalysis, and batteries. We theoretically investigate the use of Ni-doping to generate distorted 1T phases, and find not only the ones usually reported but also two further phases (3×3 and 4×4), depending on the concentration and the substitutional or adatom doping site. Corresponding pristine phases are stable after dopant removal, which might offer a potential route to experimental synthesis. We find large ferroelectric polarizations, most notably in 3×3 which – compared to the recently measured 1T'' – has 100 times greater ferroelectric polarization, a lower energy, and a larger bandgap. Doped phases include exotic multiferroic semimetals, ferromagnetic polar metals, and improper ferroelectrics with only in-plane polarization switchable. The pristine phases have unusual multiple gaps in the conduction bands, with possible applications for intermediate band solar cells, transparent conductors, and nonlinear optics.

TOC Graphic



The crystal structure of MoS₂ has several polymorphs – 2H and 3R in bulk, and in monolayers 1H and 1T – which differ by coordination around Mo: 1H has trigonal prismatic coordination in common with 2H and 3R, and 1T has octahedral bonding. 1T is higher in energy, and so most studies of monolayer MoS₂ have focused on the 1H phase. 2H-MoS₂ has shown promise in lubrication, hydrodesulfurization, and optoelectronics.^{1–4} Theoretical and experimental work has shown that doping with Ni and other transition metals in 1H- and 2H-MoS₂ can improve catalytic reactivity,^{5–7} lubrication and sliding^{8–12} and gas sensing.^{13,14} 1T-MoS₂ and its well-known distortions to reconstructed phases¹⁵ have recently been shown to have a variety of exciting properties such as topological bands,¹⁶ high nonlinear optical susceptibility,¹⁷ and ferroelectricity.¹⁸ However, much less is known about transition-metal doping in 1T-MoS₂ (as demonstrated experimentally with Ni intercalation¹⁹ and recently substitution for Mo^{20,21}) and its potential for modulating structural and electronic properties – in particular, how transition-metal doping can interact with these distortions.

1T-MoS₂ shows metallic behavior, uniquely among the polytypes of MoS₂, which are otherwise semiconducting. Applications of 1T-MoS₂ have been explored such as catalysis of the hydrogen evolution reaction,²² supercapacitors and batteries^{23,24} and photocatalysis.²⁵ Theory^{15,26} and experiments show 1T is unstable and instead is found in more stable distorted phases such as 1T' (2×1), 1T'' (2×2), 1T''' ($\sqrt{3} \times \sqrt{3}$), $\sqrt{3} \times 1$, or $2\sqrt{3} \times 2\sqrt{3}$.^{27–29} (We will mostly use the reconstruction notation $N_a \times N_b$ for clarity.) These distorted 1T phases show interesting properties: 1T' has been calculated to be a topological insulator,¹⁶ 1T''' has been predicted to be a 2D ferroelectric material³⁰ and a recent experiment showed a superior hydrogen evolution reaction activity compared to 2H-MoS₂,³¹ and 1T'' was recently demonstrated experimentally to be ferroelectric.¹⁸ Moreover, the different stackings of bulk 1T' has been found to result in topological insulators or nodal-line semimetals,³² indicating yet another degree of freedom to explore in this family of materials. Reconstructed 1T phases have been synthesized typically via intercalated alkali metal ions in 2H-MoS₂: Li intercalation and exfoliation leads to formation of 1T'³³ and 1T'',³⁴ and synthesis of KMoS₂

and deintercalation of K leads to 1T' and 1T'''.¹⁷ Intercalation with transition metals Cu, Ni, and Co has also been used to synthesize 1T phases.^{19,35} Calculations showed that adsorption of Li on 1H,³⁶ Cu adsorption on 2H,³⁷ and charge doping of 2H³⁸ or 1T³⁹ can also lead to 1T'. Other non-doping-related synthesis methods include laser writing on 2H to produce 1T' regions,⁴⁰ tensile strain on the corresponding 2H-MoTe₂ to produce 1T'-MoTe₂,⁴¹ and direct synthesis methods for 1T-MoS₂ in vapor and liquid phases.²⁸ The variety of 1T-derived phases of MoS₂, the range of remarkable properties they show, and the use of intercalation, adsorption, and charge doping for their synthesis, together suggest the possibility of using other dopants to further explore the potential phase space for 1T reconstructions, searching for novel properties as well as ways to tune or optimize known properties of 1T phases.

In this paper, we perform systematic first-principles calculations to investigate the effect of Ni-doping on 1T-MoS₂ at various concentrations, including substitutions for Mo and S as well as adsorption on different sites. We consider the most probable sites for dopants in monolayer MoS₂, including substitutions and adatoms (same as in 1H¹⁰), as shown in Fig. 1. (While adsorption may be considered a distinct process from doping, we classify it together with substitution here due to its connection with bulk intercalation and potential charge doping.⁴²) The bridge adatom site relaxes to hollow and is not considered further. We study 2×2 , 3×3 , and 4×4 supercells, each with one Ni dopant, corresponding to different doping concentrations. While an ordered doping scheme might not be necessary, it has been frequently found that high doping concentrations lead to ordered phases.^{43,44}

We compare the thermodynamic favorability via the doping formation energy, a function of the chemical potentials during growth⁴² (SI Sec. 2). Our reference is the most stable distorted phase, 1T' (2×1), which is 0.26 eV per MoS₂ unit lower in energy than 1T. The doping formation energies for Mo or S substitution and different adatom sites are shown in Figs. S1-S3. Hollow is the most favorable adatom site,⁴⁵ though Mo-atop is favored for 1H.¹⁰ Although these energies are positive, Ni doping is energetically favorable from undistorted 1T in nearly all cases due to lowering of energy by reconstructions. Substitutional doping

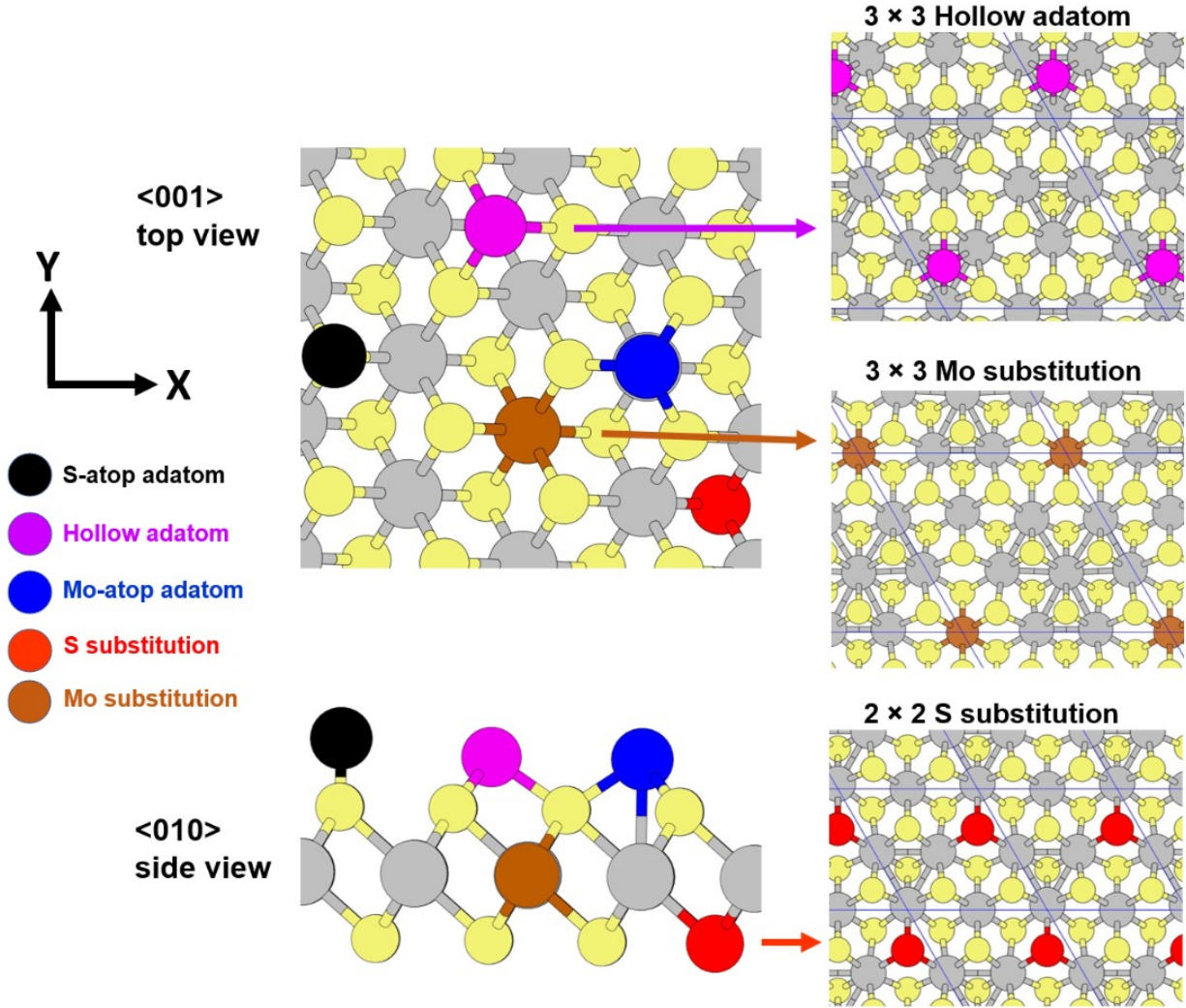


Figure 1: Left: Different doping sites for Ni in 1T-MoS₂, with definition of x and y axes. Right: Example reconstructions for different doping sites and concentrations.

formation energies are more favorable for 1T' than 1H.¹⁰ Doping lowers energy differences between 1H and 1T compared to the pristine $\Delta E = 0.85$ eV per MoS₂, but 1H remains favored (Fig. S4). Mo substitution at high concentration (8%) can bring the difference down to 0.23 eV per MoS₂ unit. The $T = 0$ phase diagram as a function of chemical potential⁴² (Fig. S5(a)) shows that in equilibrium the hollow site is most compatible with stability of 1T or 1T', but Mo and S substitution are also accessible under some conditions. We note that our previous work showed that Ni-doped MoS₂ is always above the convex hull at $T = 0$ compared to other compounds of Ni, Mo, and S.⁴² Despite this thermodynamic

unfavorability, abundant experimental evidence has been found of Ni incorporation into 2H-MoS₂,^{46,47} and more recently, 1T-MoS₂.¹⁹⁻²¹ Approaches can involve non-equilibrium conditions such as hydrothermal methods for Mo substitution, or creation of sulfur vacancies that can be filled by transition metals for S substitution.^{48,49}

Doping is found to induce different reconstructions, with various patterns of Mo-atom clustering depending on supercell size and doping scheme (Fig. 1). The DFT relaxation trajectories show that the distortions are driven by bond length changes when Ni is introduced to the structure, which not only break the symmetry but also define the local geometry. Mo atoms whose bonds to S are stretched are induced to cluster, which can in turn stretch other Mo-S bonds and induce further clustering. As in 1H-MoS₂,¹⁰ we find Ni-S bonds in Mo-substitution are shorter (2.25 Å) and Ni-Mo bonds in S-substitution are longer (2.51 Å), compared to Mo-S bonds. In Mo substitution, Ni pulls S closer, weakening neighboring Mo-S bonds and making the Mo atoms cluster. In S substitution, Ni pushes Mo farther away, causing now-closer Mo atoms to cluster. In S-atop, Ni weakens bonds from that S to Mo neighbors, causing clustering around Ni. In Mo-atop, Ni pulls S atoms closer, causing clustering away from Ni of Mo atoms with stretched bonds. In hollow, Ni pushes Mo away, causing clustering away from Ni.

Table 1: Different pristine reconstructions resulting after removal or replacement of Ni atom in different supercells of Ni-doped 1T.

Doping type	2×2	3×3	4×4
Mo subs.	2×2	3×3	4×4
S subs.	2×2	$\sqrt{3} \times \sqrt{3}$ 4B	2×2
Hollow	2×2	$\sqrt{3} \times \sqrt{3}$ 2B	2×2
Mo-atop	2×2	3×3	2×2
S-atop	2×2	$\sqrt{3} \times \sqrt{3}$ 2B	2×2

We found that the doped structures can give rise to reconstructions even of the pristine material: we reversed the doping by removing adatoms or restoring Mo or S atoms to Ni-substituted sites, and relaxed the resulting structures, finding stable distortions. This process of removal of adatoms is akin to the methods used to synthesize 1T phases via Li or

K atoms,⁵⁰ and undoing Ni substitution of Mo or S seems plausible via ion-exchange methods that have been used to interconvert different TMDs⁵¹ and produce 1T-MoS₂ nanoflowers.⁵² Therefore the route used in our calculations may also constitute a viable method for experimental synthesis, though stabilization by epitaxy⁵³ or ligands⁵⁴ are also possible strategies. Most of the structures relaxed to previously known phases (2×2 or $\sqrt{3} \times \sqrt{3}$)^{15,26,27,38} while a few reconstructions were not found in the literature (Table 1, Fig. 2). Note that the supercell size constrains the possible reconstructions: e.g. 2×2 can form only from 2×2 or 4×4 , and $\sqrt{3} \times \sqrt{3}$ only from 3×3 . We did not find 2×1 but include it in further analysis for comparison. The properties of the pristine reconstructions are shown in Table 2. Lattice parameters and Mo-Mo distances are consistent with Zhuang et al.³⁸ We find there are two different $\sqrt{3} \times \sqrt{3}$ structures, with the same C_{3v} symmetry (but different locations of the C_3 axis) and all 3 Mo atoms equivalent at the Wyckoff c positions. They have different numbers of bonds from Mo to other Mo atoms, so we will distinguish them as 2B and 4B. The distinction between these structures does not seem to have been appreciated previously: $\sqrt{3} \times \sqrt{3}$ in Zhuang et al.³⁸ is 2B whereas in Fang et al.¹⁷ it is 4B. The phases not previously reported are obtained from 3×3 and 4×4 Mo substitution, and the energies are 0.24 eV and 0.15 eV per MoS₂ lower than 1T, respectively. Note that 3×3 is more stable than the experimentally established 2×2 .¹⁸ The most stable structure seen is $\sqrt{3} \times \sqrt{3}$ 4B, which has been synthesized experimentally¹⁷ with lattice parameter $a = b = 5.58$ Å and Mo-Mo bond length 3.01 Å, close to our results of 5.61 Å and 3.02 Å. Space groups and point groups of the structures are given in Table S3. We confirmed that similar results are obtained for the relative energies and structural parameters using PBE+ U ⁵⁵ or the PBE0 hybrid functional^{56,57} (Table S4).

These structures are distorted out of plane as well: S atoms vary in their z -height (Fig. 3), a symmetry-breaking which allows out-of-plane polarization. There has been little attention in distorted 1T to this z -variation,^{15,17,27,30,38} and only recently has it been connected to polarization in the 2×2 structure.¹⁸ The variations for 3×3 are largest, and as shown below,

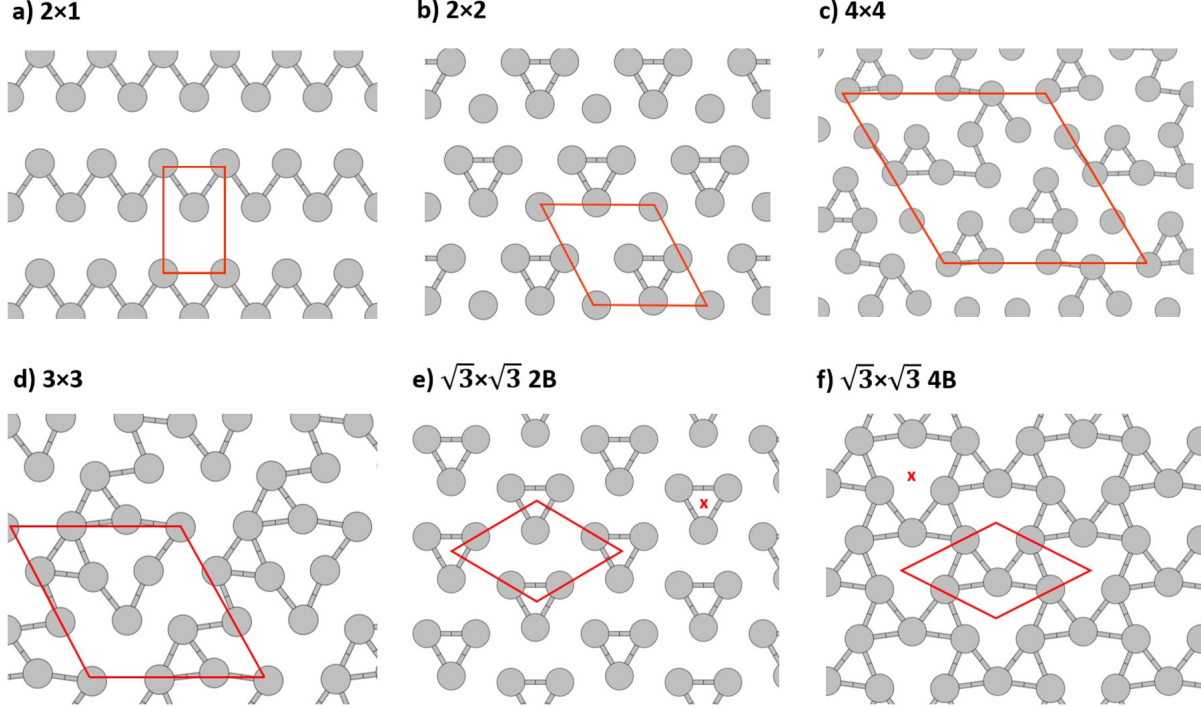


Figure 2: Mo clustering for different reconstructions. S atoms are not shown, for clarity. All Mo-Mo bonds shorter than 3.08 Å, twice the covalent radius of Mo,⁵⁸ are shown. There are several inequivalent bond lengths in 3×3 and 4×4 . The red \times in (e) and (f) denotes the location of the C_3 axis.

it has the largest ferroelectric polarization. While the maximum displacements are similar on the two sides, there is a net polarization because the patterns are different, and there can be significant variation in dynamical charges among S atoms in 1T-MoS₂ phases.^{18,59} In $\sqrt{3} \times \sqrt{3}$ 2B and 4B, the z -height of S atoms varies on one side and is constant on the other, whereas in all other structures, we find variations on both sides. The pattern of z -variation in 2B and 4B is opposite: in 2B, lines of S atoms consist of pairs closer to the Mo plane separated by an atom farther; whereas in 4B there are pairs farther, separated by an atom closer. The variation on only one side in $\sqrt{3} \times \sqrt{3}$ is connected to the fact that these reconstructions only occur from an adatom or S substitution, which breaks the symmetry between the sides, but not from Mo substitution. We find Ni substituting S causes sites to move closer to the Mo plane, and Ni on S-atop and Mo-atop sites moves S farther from Mo. Ni on the hollow site moves some S atoms closer and some farther, on both sides. The

S atoms centered in Mo triangular clusters are always farthest from the Mo plane. These vertical corrugations are consistent with previously calculated structures of $\sqrt{3} \times \sqrt{3}$ 4B in Fang et al.¹⁷, 2×2 in Lipatov et al.¹⁸, and $\sqrt{3} \times \sqrt{3}$ 2B (in plane³⁸ and out of plane⁶⁰). This surface non-uniformity could be interesting for surface chemistry or catalysis as it may tune reactivity: in 1T' the reactivity for chemisorption is higher for S atoms closer to the Mo plane.⁶¹

The pristine reconstructions result from relaxation of a structure whose symmetry was broken by the presence of the Ni dopants, which indicates a minimum level of stability. The dynamical stability of all reconstructions was further investigated by calculating phonon bandstructures, as shown in Fig. S13. We found structures 2×1 , 3×3 , and $\sqrt{3} \times \sqrt{3}$ 4B to be dynamically stable. However, in several cases instabilities were found – real in the case of $\sqrt{3} \times \sqrt{3}$ 2B and 3×3 , but attributed to numerical issues⁶² in the case of 2×1 , 2×2 and 4×4 . The instabilities were investigated by displacing the atomic coordinates in the direction of the imaginary-frequency displacement eigenvectors scaled by 0.01 Å, and then relaxing the atomic structure and lattice.⁶² The higher-energy $\sqrt{3} \times \sqrt{3}$ structure (2B)³⁸ was found to be unstable, with imaginary frequencies at Γ , M and K. Relaxation after displacement by the imaginary mode at Γ yielded $\sqrt{3} \times \sqrt{3}$ 4B. We nonetheless retained $\sqrt{3} \times \sqrt{3}$ 2B structure in our data set due to interesting properties such as a higher ferroelectric polarization (see below), and the possibility that it might be stabilized by temperature, epitaxy,⁵³ ligands,⁵⁴ or other factors. Our originally obtained 3×3 structure (Fig. S14), which is 0.08 eV lower in energy than undistorted 1T, proved to be unstable, and relaxation after displacement led to the significantly more stable 3×3 structure analyzed in the text. In the case of 2×2 , we found a small imaginary frequency at Γ which corresponds to a flexural mode (Fig. S15), notoriously difficult to calculate accurately in DFT.⁶³ Relaxation after displacement returned to the original structure, showing that the instability is a numerical artifact, which is consistent with the realization in experiment of this phase.¹⁸ 2×1 shows a similar flexural instability at Γ , which we did not investigate further, since it is included here only for

Table 2: Structure, energy, and DFT bandstructure properties of pristine reconstructions of 1T.*

a)

Structure	a, b (Å)	d (Å)	Δz (Å)	ΔE (eV)	E_g (eV)
1×1	3.18	3.18	0, 0	0	0
2×1	5.67, 3.18	2.78	0.39, 0.39	-0.26	0.02
2×2	6.43	2.78	0.27, 0.25	-0.21	0.08
3×3	9.70	2.93	0.47, 0.51	-0.24	0.71
$\sqrt{3} \times \sqrt{3}$ 2B	5.64	2.84	0, 0.17	-0.19	0.59
$\sqrt{3} \times \sqrt{3}$ 4B	5.61	3.02	0, 0.44	-0.26	0.83
4×4	13.01	2.78	0.32, 0.31	-0.15	0.25

b)

Structure	Bandgap (eV)	ΔE_{VBM} (eV)	N_{bands}
	0.46	1.63	2
1×1	0.58	3.98	2
2×1	0.30	4.81	8
	0.19	0.81	2
2×2	0.15	1.92	3
	0.52	4.52	11
	0.10	1.63	9
3×3	0.42	4.72	27
	0.83	1.20	3
$\sqrt{3} \times \sqrt{3}$ 2B	0.22	2.54	3
	0.73	4.40	6
	0.22	1.70	3
$\sqrt{3} \times \sqrt{3}$ 4B	0.38	4.89	9
4×4	0.11	1.84	17
	0.39	4.69	47

* a) Structure, energy, and gap; a, b are the lattice parameters ($a = b$ in most cases); d is the shortest Mo-Mo distance, characterizing clustering; Δz gives the range of vertical positions of S atoms, for each of the two sides; ΔE is the energy difference per MoS₂ with respect to undistorted 1T. b) Conduction-band gaps: ΔE_{VBM} is the energy difference of the bottom of the gap from the valence band maximum (VBM); N_{bands} is the number of bands from the previous gap up to this gap.

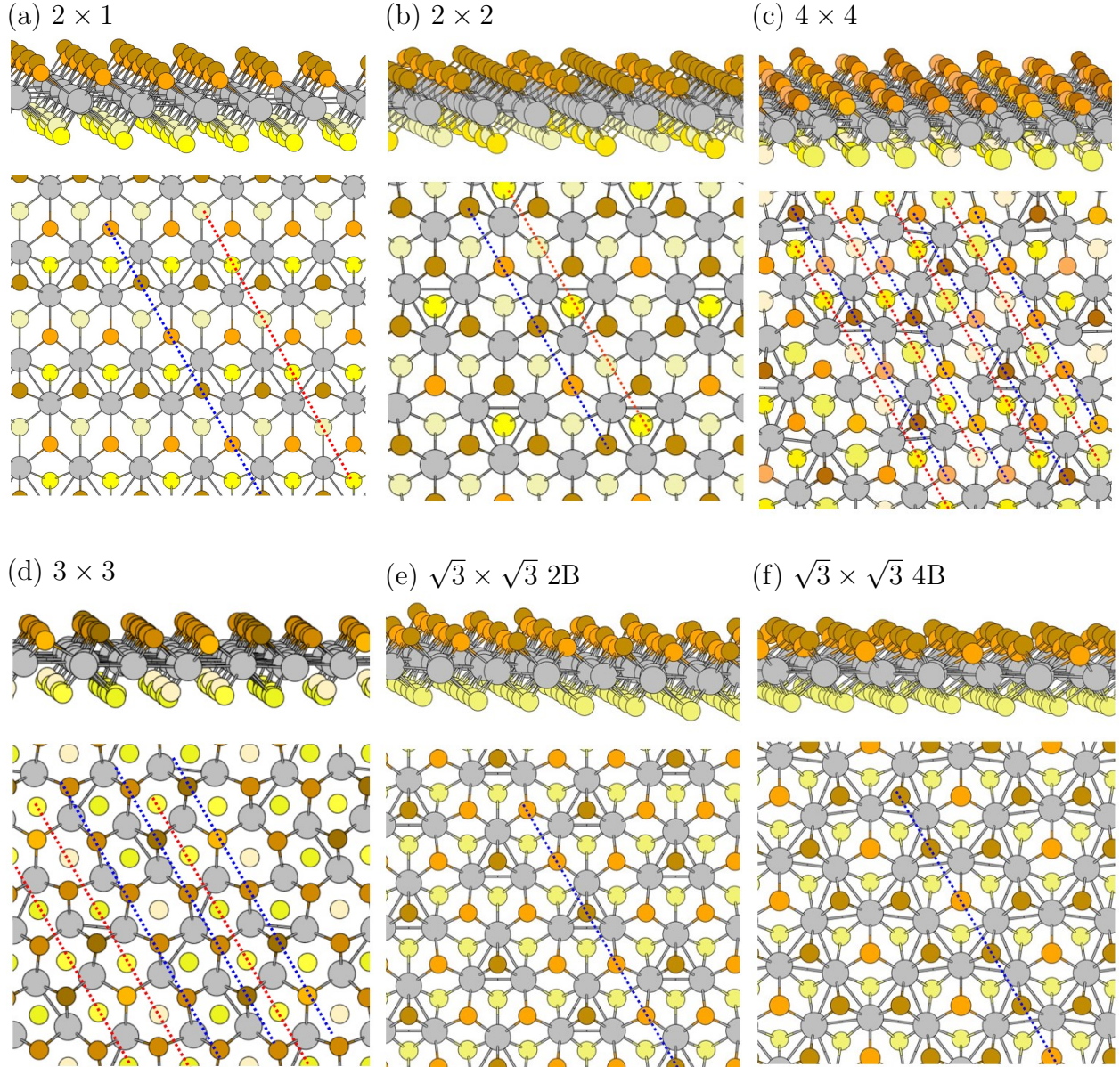


Figure 3: Structures in side and top views, showing vertical corrugation of S atoms. Orange and yellow colors are used to represent S atoms on the top and bottom of the Mo-plane, respectively. Darker color indicates greater distance from the Mo-plane. Blue and red dotted lines indicate directions along which S atoms heights vary for top and bottom S atoms, respectively.

comparison to the phases resulting from Ni-doping, and the existence of this $1T'$ phase is well established experimentally^{17,33,40} and theoretically.^{38,64} For 4×4 , relaxation in a 2×1 supercell after displacement by imaginary modes corresponding to the M point led back to

the original structure, indicating no true instability. These modes also have flexural character (Fig. S15). We conclude that the 2×2 and 4×4 structures are indeed dynamically stable.

We found a variety of electronic structures in pristine and Ni-doped reconstructions. For pristine phases, band gaps are shown in Table 2, density of states (DOS) in Fig. S6, and bandstructures in Fig. 4. For Ni-doped phases, the band gaps are in Table S1, DOS in Fig. S7 and bandstructures in Fig. S9. The pristine 1T phase is metallic,^{65,66} but becomes semiconducting with most distortions due to a Jahn-Teller mechanism.¹⁵ This occurred with doping in most cases we considered; only Mo-substituted 2×2 and 3×3 , S-substituted 4×4 , and S-atop 2×2 and 4×4 remained metallic. All of the pristine reconstructions obtained from the doped ones are semiconducting, albeit with a very small gap in 2×1 , as in Hu et al.⁶⁴ We calculated the \mathbb{Z}_2 topological index of the pristine and doped reconstructions using Z2Pack,^{67,68} but found them to be topologically trivial, other than 2×1 .¹⁶ We did however notice other unusual features in the bandstructures of the pristine phases: there are multiple gaps in the conduction bands (Table 2(b), Fig. 4). Undistorted 1T has two conduction-band gaps even though it is metallic (Fig. S8a). Only rarely have bandstructures been published extending high enough in energy to see these gaps,⁶⁹ and they do not seem to have been discussed in the literature. These gaps are preserved or increase in number in distorted phases (except 2×1). DOS plots (Figs. S6-S7) confirm the presence of these gaps. We note that while in general the fundamental gap is underestimated by PBE, other aspects of the bandstructure are typically well estimated. We verified that PBE+ U and spin-orbit coupling do not significantly change the bandstructure (e.g. Fig. S11). In all calculated structures, a gap of 0.3–0.7 eV exists ~ 5 eV above the VBM, between bands of mostly Mo d character below and Mo s character above (Fig. S8b). A similar gap ~ 5 eV above the VBM is found in ReS₂ bilayers, between Re d and Re s bands, as probed by time-resolved second harmonic generation.⁷⁰ Similar second gaps are reported in other metal chalcogenides.^{71,72} However, the other gaps found in 1T distorted phases are quite unusual, and there does not seem to be a standard explanation for such gaps.

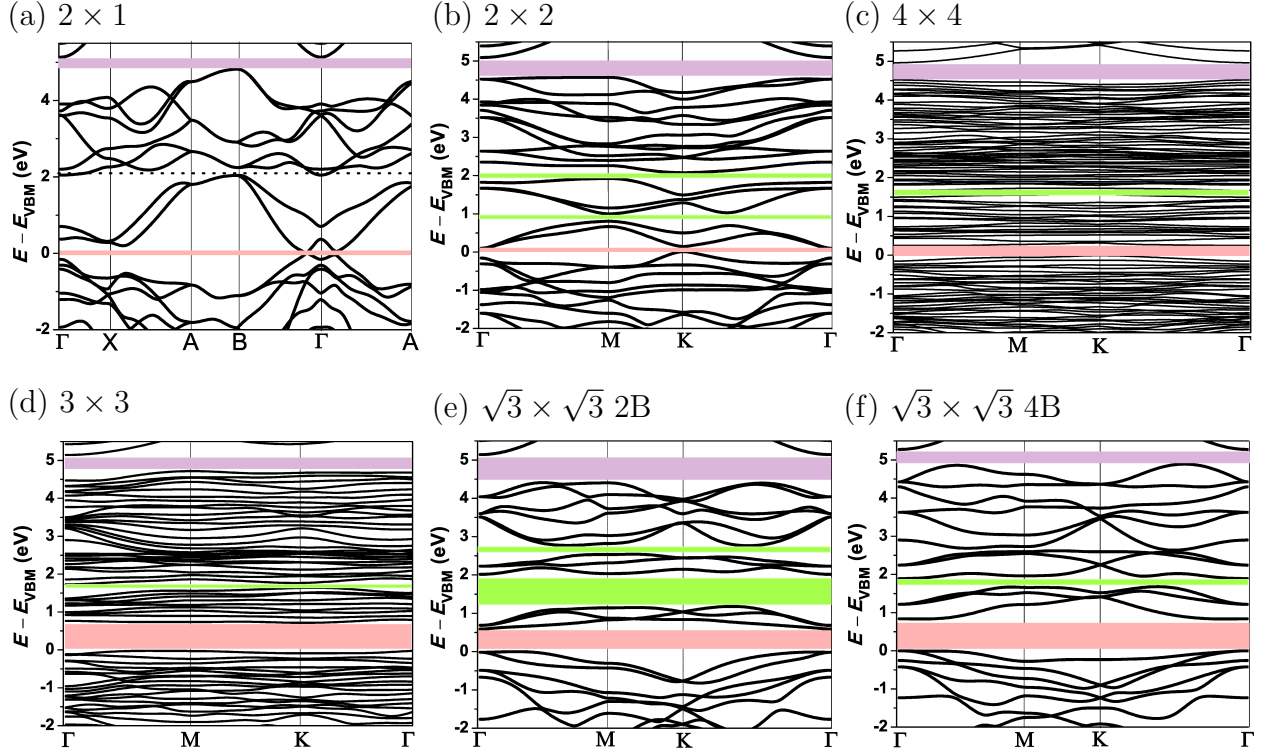


Figure 4: Electronic bandstructure of pristine reconstructed structures, in the Brillouin zone of each structure’s primitive cell. The colored stripes highlight the gaps, with pink as the fundamental band gap, purple as a gap common to all structures due to transition between Mo s and d -orbitals, and green for gaps in between those two. The dotted line in a) shows the small band overlap at this energy.

The origin of these gaps is complex. The gaps are induced by perturbations to the potential felt by the electrons at the reconstructed supercell periodicity, as for mini-bands in superlattices,⁷³ with the perturbation provided by Mo clustering. What explains the patterns in different structures? The gaps are not due to a transition between different types of orbitals as they are within bands all due to Mo d and S p -orbitals. We examined the wavefunctions of band complexes between gaps, and we find some common patterns. Some gaps are transitions between bands localized on clustered and non-clustered Mo orbitals. In $\sqrt{3} \times \sqrt{3}$ 2B and 4B, we see Hückel-type patterns of bonding, non-bonding, and anti-bonding among d -orbitals in a band complex. We examined local symmetries of Mo atoms for crystal field splitting (Table S3), and find mostly symmetry elements (C_1, C_{2v}) that break

the degeneracy of d_{xz} and d_{yz} , and $d_{x^2-y^2}$ and d_{xy} . This breaking of degeneracy contributes to gap openings, and some of the gaps are found to be transitions between different crystal-field-split d -orbital shapes. In the simplest case of undistorted 1T, the gap around 2 eV above the Fermi energy has mostly d_{z^2} character below and mostly d_{xz} and d_{yz} above (Fig. S8b). We do not see any clear correlation between the multiple gap patterns and the overall symmetry, number of inequivalent Mo atoms, or symmetry of the Mo sublattice. In a tight-binding picture, loss of symmetry can increase the variation of on-site energies; for small hoppings (and bandwidths), this could open up gaps, but for large hoppings, it could overlap bands and close gaps. We investigated the Löwdin charges on Mo atoms and found significant variation (Fig. S12), which would correlate with on-site energies, but there is no clear correlation of the charges with number or magnitude of gaps. Ultimately we conclude that the gaps, and the number of bands between them, are due to a complex interplay of reconstructed periodicity, Mo cluster bonding, crystal-field splitting, and overall symmetry. Wannier-function-based analysis⁷⁴ may shed further light on the mechanisms.

These multiple gaps could possibly be utilized in intermediate band solar cells (IBSCs),⁷⁵ a third-generation photovoltaic concept which can exceed the Shockley-Queisser limit by allowing the voltage to be increased without losing absorption. In IBSCs, electrons can be excited from the valence band across a first band gap to an intermediate band (from which recombination is slow), and then excited again across a second band gap. Whereas in a standard solar cell the single band gap controls both the voltage and the absorption, here the resulting voltage is related to the sum of the two band gaps. Such intermediate bands for solar cells are typically due to dopants,^{76,77} which can however cause undesired scattering and recombination. In our case, however, we have multiple gaps even in the pristine phases due to reconstruction. Ideally, an IBSC should have a partially filled intermediate band, to facilitate electronic transitions,⁷⁸ which could be obtained by electrostatic gating, or realized by some of the Ni-doped structures (Fig. S9 (b,d)) that have metallic intermediate bands. Multiple gaps, in particular in the metallic cases or with gating, could also be applied for transparent

conducting materials (TCMs)⁷⁹ – in some successful TCMs, the bandstructure has a partially filled conduction band, providing conductivity, with a large second gap above it, providing transparency. As with IBSCs, such bandstructures have typically been provided by doping, but here could be realized in an undoped system which may have better mobility. A final application is nonlinear optics, as studied for ReS₂,⁷⁰ since multiple gaps enable multiple simultaneous resonances for sum- or difference-frequency generation. Phases studied here are noncentrosymmetric and therefore have nonzero $\chi^{(2)}$, as has been shown for $\sqrt{3} \times \sqrt{3}$ 4B¹⁷ and 2×2 .¹⁸

We find spontaneous polarization in the reconstructions. Pristine $\sqrt{3} \times \sqrt{3}$ 4B has been calculated to be ferroelectric with an equivalent bulk polarization of $0.18 \mu\text{C}/\text{cm}^2$ (using the S-S distance as the height along the z -direction).³⁰ Recently the out-of-plane polarization for a bulk 2×2 with layer height of 5.96 \AA was calculated¹⁸ to be $0.04 \mu\text{C}/\text{cm}^2$ (we obtain $0.06 \mu\text{C}/\text{cm}^2$). We will focus on the polarization per unit area as befitting a monolayer 2D material. We calculate polarization magnitudes of: 2×2 , $4.06 \times 10^{-4} e/\text{\AA}$; $\sqrt{3} \times \sqrt{3}$ 4B, $7.18 \times 10^{-4} e/\text{\AA}$ (consistent with Shirodkar and Waghmare³⁰); $\sqrt{3} \times \sqrt{3}$ 2B, $2.19 \times 10^{-3} e/\text{\AA}$ ($3 \times$ larger than 4B); 4×4 , $1.34 \times 10^{-2} e/\text{\AA}$; and 3×3 , $5.37 \times 10^{-2} e/\text{\AA}$. The polarizations are in the $-z$ direction for our $\sqrt{3} \times \sqrt{3}$ 2B and $\sqrt{3} \times \sqrt{3}$ 4B structures, as in-plane polarization is forbidden in C_{3v} . There is in-plane polarization for 2×2 (C_s), 3×3 (C_1) and 4×4 (C_1), with polarization vectors $(3.45, 0, 2.15) \times 10^{-4} e/\text{\AA}$, $(380, -380, -1.76) \times 10^{-4} e/\text{\AA}$, and $(126, -44.3, -3.07) \times 10^{-4} e/\text{\AA}$, respectively. These 3×3 and 4×4 structures' polarizations are 132 and 33 times larger than 2×2 . Using the bulk 2×2 layer height, these correspond to bulk polarizations of $\sim 8 \mu\text{C}/\text{cm}^2$ and $\sim 2 \mu\text{C}/\text{cm}^2$ respectively, only one order of magnitude smaller than standard ferroelectrics PbTiO₃ ($79 \mu\text{C}/\text{cm}^2$) and PbZrO₃ ($70 \mu\text{C}/\text{cm}^2$).⁸⁰ For comparison, 2×1 has zero polarization due to C_{2h} symmetry. We can make a simple estimate of ferroelectric switching, considering coherent reversal via the (paraelectric) undistorted 1T structure,⁸⁰ and using the energy differences in Table 2. We obtain barriers of 0.03–0.09 eV/atom, comparable to PbTiO₃ (~ 0.01 eV/atom) and PbZrO₃ (~ 0.04 eV/atom).⁸⁰ More-

over, there could be a lower-energy switching pathway. Out-of-plane polarization switching was recently observed in an experiment¹⁸ for the 2×2 structure, for which we estimate a barrier of 0.21 eV. Since all of the structures have similar or lower barriers, these results suggest the polarization is switchable in those cases too. The experimental results suggest that monolayer ferroelectric properties can be retained when stacked into a multilayers, for potential nanoelectronic devices.

We investigated magnetism in doped structures, given its presence in some structures of doped 1H-MoS₂.^{10,81} We found 3 ferromagnetic cases and 1 antiferromagnetic case, with moments on the Ni site (Table 3, Table S2). We estimated Curie temperatures with mean-field theory (SI Sec. 1), and find high T_C for the metals. Metals cannot have polarization in a periodic direction, but two of these cases have out-of-plane polarization, making them ferromagnetic polar metals.⁸² Note that 2×2 was calculated and measured to be a polar metal as well¹⁸ but only in the bulk, not monolayers. We also have unusual ferromagnetic and antiferromagnetic semimetals,^{83,84} which have both out-of-plane and in-plane polarization, making them (anti)ferromagnetic-ferroelectric multiferroics, rarely reported in 2D.^{85,86} Polarization for all doped structures is in Table S1. The in-plane polarization is switchable via undistorted 1T where it is zero by symmetry, with switching energies per atom comparable to the pristine phases, and there could be other lower-barrier pathways. Doped structures (except for Mo substitution) have out-of-plane polarization due mainly to Ni (with oxidation state 2-, SI Sec. 1) rather than distortion, which therefore cannot be feasibly switched. Mo substitution has switchable (though small) polarization since the undistorted 1T is centrosymmetric. The other cases are an unusual kind of improper ferroelectric controlled by in-plane distortion,⁸⁷ where only the in-plane polarization (up to $\sim 10^{-3}$ e/Å) is switchable. We note this type is distinct from recently reported ferroelectric doped 2D materials, which switch via interlayer sliding rather than intralayer distortions.⁸⁸

In conclusion, we found that Ni-doping 1T MoS₂ induces a panoply of different reconstructions with Mo clustering, due to the effect of Ni on neighboring bonds. Removing or

Table 3: Magnetic doped structures.^a

Doping type	μ (μ_B)	ΔE_{mag} (meV)	T_C (K)	Type	Polarization ($e/\text{\AA}$)
2×2 S subs.	0.05	-0.19	19.6	semimetal	$(-1.06, 1.18, -3.06) \times 10^{-3}$
4×4 S subs.	0.78	-27.91	493	metal	$(0, 0, -6.60) \times 10^{-4}$
2×2 S-atop	0.30	-17.32	485	metal	$(0, 0, -1.14) \times 10^{-2}$
3×3 S-atop	0 [0.07]	-0.09	-	semimetal	$(6.08, -6.08, -49.3) \times 10^{-4}$

^a Moment μ per Ni atom and energy difference ΔE_{mag} per Ni atom of spin-polarized state *vs.* the non-spin-polarized paramagnetic state. Moment in square brackets for 3×3 S-atop is the integrated absolute magnetization, indicating weak antiferromagnetism.

replacing the dopant and relaxing (and adding a small perturbation in some cases) leads to pristine reconstructions are dynamically stable. These resulting phases include not only the typically reported ones but also 3×3 and 4×4 . Two versions of $\sqrt{3} \times \sqrt{3}$ with two and four Mo-Mo bonds are present initially, but only the latter is dynamically stable. These structures show large ferroelectric polarizations and low switching barriers. Most notably, compared to the experimentally measured 2×2 ,¹⁸ 3×3 has polarization higher by two orders of magnitude, is more stable, and has a significantly larger band gap, which reduces difficulties with charge leakage and conductivity. Most Ni-doped structures are semiconductors but they also include unusual ferromagnetic polar metals, multiferroic semimetals, and in-plane improper ferroelectrics. Pristine and doped phases showed multiple gaps in the conduction bands, a phenomenon which has potential application in intermediate band solar cells, transparent conducting materials, and nonlinear optics. Our calculations suggest that Ni-doping of 1T-MoS₂ (perhaps including intercalation) could be a way to synthesize a range of distorted pristine phases, by removing or replacing dopants through methods such as dissolution or evaporation of adatoms or intercalants,⁵⁰ or ion exchange for Mo or S substitution.^{51,52} Other possible techniques are epitaxy on a Ni-doped monolayer or other suitable substrate;⁵³ or stabilization with appropriate ligands.⁵⁴ Experiments have shown that 1T phases can be stable even under reaction conditions of ion exchange⁵² or etching of S atoms.³¹ Such structures, including the potential analogues involving other transition-metal dichalcogenides and transition-metal dopants, are interesting for applications in electronics,

optics, energy storage, and catalysis, and may offer other intriguing properties.

Computational Methods

Our calculations use density functional theory (DFT) in the plane-wave pseudopotential code Quantum ESPRESSO.⁸⁹ Further details are given in SI Sec. 1. We use the PBE exchange-correlation functional⁹⁰ and Grimme-D2⁹¹ van der Waals correction for consistency with bulk calculations (SI Sec. 2), except for formation energies with respect to Mo and Ni, for which we use PBE alone.⁴² Polarization is calculated with the dipole correction method⁹² out of plane, and Berry-phase method⁹³ in plane. Phonon bandstructures to assess dynamical stability were calculated by density-functional perturbation theory.⁹⁴ We work with neutral systems, periodic in plane but separated by vacuum out of plane.

Acknowledgments

We acknowledge Enrique Guerrero for preparing the phase diagram. This work was supported by UC Merced start-up funds and the Merced nAnomaterials Center for Energy and Sensing (MACES), a NASA-funded research and education center, under awards NNX15AQ01 and NNH18ZHA008CMIROG6R. This work used computational resources from the Multi-Environment Computer for Exploration and Discovery (MERCED) cluster at UC Merced, funded by National Science Foundation Grant No. ACI-1429783, and the National Energy Research Scientific Computing Center (NERSC), a U.S. Department of Energy Office of Science User Facility operated under Contract No. DE-AC02-05CH11231.

Supplementary Information

Computational details; analysis of formation energies; full structural, electronic, polarization, and magnetic properties of Ni-doped 1T-MoS₂; doping formation energies as a function

of concentration; doped bandstructures; doped and pristine density of states; and further information on phonon bandstructure and dynamical instabilities (PDF). PBE+Grimme-D2 relaxed coordinates for Ni-doped 1T MoS₂ and reconstructed pristine 1T structures, in XCrySDen format (ZIP).

References

- (1) Mao, J.; Wang, Y.; Zheng, Z.; Deng, D. The rise of two-dimensional MoS₂ for catalysis. *Front. Phys.* **2018**, *13*, 138118.
- (2) Radisavljevic, B.; Radenovic, A.; Brivio, J.; Giacometti, V.; Kis, A. Single-layer MoS₂ transistors. *Nat. Nanotech.* **2011**, *6*, 147–150.
- (3) Lopez-Sanchez, O.; Lembke, D.; Kayci, M.; Radenovic, A.; Kis, A. Ultrasensitive photodetectors based on monolayer MoS₂. *Nat. Nanotech.* **2013**, *8*, 497–501.
- (4) Krause, O.; Müller, F.; Birkmann, S.; Böhm, A.; Ebert, M.; Grözinger, U.; Henning, T.; Hofferbert, R.; Huber, A.; Lemke, D.; Rohloff, R.-R.; Scheithauer, S.; Gross, T.; Fischer, T.; Luchtel, G.; Merkle, H.; Übele, M.; Wieland, H.-U.; Amiaux, J.; Jager, R.; Glauser, A.; Parr-Burman, P.; Sykes, J. High-precision cryogenic wheel mechanisms of the JWST/MIRI instrument: performance of the flight models. *SPIE* **2010**, *7739*, 773918.
- (5) Jeong, G.; Kim, C. H.; Hur, Y. G.; Han, G.-H.; Lee, S. H.; Lee, K.-Y. Ni-Doped MoS₂ Nanoparticles Prepared via Core–Shell Nanoclusters and Catalytic Activity for Upgrading Heavy Oil. *Energy Fuels* **2018**, *32*, 9263–9270.
- (6) Hakala, M.; Kronberg, R.; Laasonen, K. Hydrogen adsorption on doped MoS₂ nanostructures. *Sci. Rep.* **2017**, *7*, 15243.

- (7) Ma, X.; Li, J.; An, C.; Feng, J.; Chi, Y.; Liu, J.; Zhang, J.; Sun, Y. Ultrathin Co(Ni)-doped MoS₂ nanosheets as catalytic promoters enabling efficient solar hydrogen production. *Nano Research* **2016**, *9*, 2284–2293.
- (8) Jun-Feng, Y.; Braham, P.; Qian-Feng, F. Tribological properties of transition metal di-chalcogenide based lubricant coatings. *Front. Mater. Sci.* **2012**, *6*, 116–127.
- (9) Vazirisereshk, M. R.; Martini, A.; Strubbe, D. A.; Baykara, M. Z. Solid Lubrication with MoS₂: A Review. *Lubricants* **2019**, *7*, 57.
- (10) Karkee, R.; Guerrero, E.; Strubbe, D. A. Enhanced interlayer interactions in Ni-doped MoS₂, and structural and electronic signatures of doping site. *Phys. Rev. Materials* **2021**, *5*, 074006.
- (11) Guerrero, E.; Strubbe, D. A. Atomistic Mechanisms of Sliding in Few-Layer and Bulk Doped MoS₂. *arXiv:2209.15629* **2022**,
- (12) Acikgoz, O.; Guerrero, E.; Yanilmaz, A.; Dagdeviren, O. E.; Çelebi, C.; Strubbe, D. A.; Baykara, M. Z. Intercalation leads to inverse layer dependence of friction on chemically doped MoS₂. *Nanotechnology* **2022**, *34*, 015706.
- (13) Ma, D.; Ju, W.; Li, T.; Zhang, X.; He, C.; Ma, B.; Lu, Z.; Yang, Z. The adsorption of CO and NO on the MoS₂ monolayer doped with Au, Pt, Pd, or Ni: A first-principles study. *Appl. Surf. Sci.* **2016**, *383*, 98 – 105.
- (14) Tedstone, A. A.; Lewis, D. J.; O’Brien, P. Synthesis, Properties, and Applications of Transition Metal-Doped Layered Transition Metal Dichalcogenides. *Chem. Mater.* **2016**, *28*, 1965–1974.
- (15) Zhao, W.; Pan, J.; Fang, Y.; Che, X.; Wang, D.; Bu, K.; Huang, F. Metastable MoS₂: Crystal Structure, Electronic Band Structure, Synthetic Approach and Intriguing Physical Properties. *Chem. Eur. J.* **2018**, *24*, 15942–15954.

- (16) Qian, X.; Liu, J.; Fu, L.; Li, J. Quantum spin Hall effect in two-dimensional transition metal dichalcogenides. *Science* **2014**, *346*, 1344–1347.
- (17) Fang, Y.; Hu, X.; Zhao, W.; Pan, J.; Wang, D.; Bu, K.; Mao, Y.; Chu, S.; Liu, P.; Zhai, T.; Huang, F. Structural Determination and Nonlinear Optical Properties of New 1T^{'''}-Type MoS₂ Compound. *J. Am. Chem. Soc.* **2019**, *141*, 790–793.
- (18) Lipatov, A.; Chaudhary, P.; Guan, Z.; Lu, H.; Li, G.; Crégut, O.; Dorkenoo, K. D.; Proksch, R.; Cherifi-Hertel, S.; Shao, D.-F.; Tsymbal, E. Y.; Íñiguez, J.; Sinitskii, A.; Gruverman, A. Direct observation of ferroelectricity in two-dimensional MoS₂. *npj 2D Mater. Appl.* **2022**, *6*, 18.
- (19) Attanayake, N. H.; Thenuwara, A. C.; Patra, A.; Aulin, Y. V.; Tran, T. M.; Chakraborty, H.; Borguet, E.; Klein, M. L.; Perdew, J. P.; Strongin, D. R. Effect of Intercalated Metals on the Electrocatalytic Activity of 1T-MoS₂ for the Hydrogen Evolution Reaction. *ACS Energy Lett.* **2018**, *3*, 7–13.
- (20) Wang, G.; Zhang, G.; Ke, X.; Chen, X.; Chen, X.; Wang, Y.; Huang, G.; Dong, J.; Chu, S.; Sui, M. Direct Synthesis of Stable 1T-MoS₂ Doped with Ni Single Atoms for Water Splitting in Alkaline Media. *Small* **2022**, *18*, 2107238.
- (21) Luo, R.; Luo, M.; Wang, Z.; Liu, P.; Song, S.; Wang, X.; Chen, M. The atomic origin of nickel-doping-induced catalytic enhancement in MoS₂ for electrochemical hydrogen production. *Nanoscale* **2019**, *11*, 7123.
- (22) Ambrosi, A.; Soferb, Z.; Pumera, M. 2H → 1T phase transition and hydrogen evolution activity of MoS₂, MoSe₂, WS₂ and WSe₂ strongly depends on the MX₂ composition. *Chem. Commun.* **2015**, *51*, 8450–8453.
- (23) Acerce, M.; Voiry, D.; Chhowalla, M. Metallic 1T phase MoS₂ nanosheets as supercapacitor electrode materials. *Nat. Nanotech.* **2015**, *10*, 313–318.

- (24) Geng, X.; Jiao, Y.; Han, Y.; Mukhopadhyay, A.; Yang, L.; Zhu, H. Freestanding Metallic 1T MoS₂ with Dual Ion Diffusion Paths as High Rate Anode for Sodium-Ion Batteries. *Adv. Funct. Mater.* **2017**, *27*, 1702998.
- (25) Du, P.; Zhu, Y.; Zhang, J.; Xu, D.; Peng, W.; Zhang, G.; Zhang, F.; Fan, X. Metallic 1T phase MoS₂ nanosheets as a highly efficient co-catalyst for the photocatalytic hydrogen evolution of CdS nanorods. *RSC Adv.* **2016**, *6*, 74394–74399.
- (26) Ge, Y.; Wan, W.; Ren, Y.; Liu, Y. Large thermoelectric power factor of high-mobility transition-metal dichalcogenides with 1T'' phase. *Phys. Rev. Res.* **2020**, *2*, 013134.
- (27) Pal, B.; Singh, A.; G., S.; Mahale, P.; Kumar, A.; Thirupathaiah, S.; Sezen, H.; Amati, M.; Gregoratti, L.; Waghmare, U. V.; Sarma, D. D. Chemically exfoliated MoS₂ layers: Spectroscopic evidence for the semiconducting nature of the dominant trigonal metastable phase. *Phys. Rev. B* **2017**, *96*, 195426.
- (28) Sokolikova, M. S.; Mattevi, C. Direct synthesis of metastable phases of 2D transition metal dichalcogenides. *Chem. Soc. Rev.* **2020**, *49*, 3952.
- (29) Heising, J.; Kanatzidis, M. G. Exfoliated and Restacked MoS₂ and WS₂: Ionic or Neutral Species? Encapsulation and Ordering of Hard Electropositive Cations. *J. Am. Chem. Soc.* **1999**, *121*, 11720–11732.
- (30) Shirodkar, S. N.; Waghmare, U. V. Emergence of Ferroelectricity at a Metal-Semiconductor Transition in a 1T Monolayer of MoS₂. *Phys. Rev. Lett.* **2014**, *112*, 157601.
- (31) Guo, X.; Song, E.; Zhao, W.; Xu, S.; Zhao, W.; Lei, Y.; Fang, Y.; Liu, J.; Huang, F. Charge self-regulation in 1T'''-MoS₂ structure with rich S vacancies for enhanced hydrogen evolution activity. *Nat. Commun.* **2022**, *13*, 5954.

- (32) Guo, Z.; Hao, X.; Dong, J.; Li, H.; Gong, Y.; Yang, D.; Liao, J.; Chu, S.; Li, Y.; Li, X.; Chen, D. Prediction of topological nontrivial semimetals and pressure-induced Lifshitz transition in 1T'-MoS₂ layered bulk polytypes. *Nanoscale* **2020**, *12*, 22710–22717.
- (33) Eda, G.; Fujita, T.; Yamaguchi, H.; Voiry, D.; Chen, M.; Chhowalla, M. Coherent Atomic and Electronic Heterostructures of Single-Layer MoS₂. *ACS Nano* **2012**, *6*, 7311–7317.
- (34) Dungey, K. E.; Curtis, M. D.; Penner-Hahn, J. E. Structural Characterization and Thermal Stability of MoS₂ Intercalation Compounds. *Chem. Mater.* **1998**, *10*, 2152–2161.
- (35) Li, M.; Selvarajan, P.; Wang, S.; Wan, T.; Xi, S.; Wang, X.; Xue, J.; Indirathankam, S. C.; Geng, X.; Qiao, L.; Vinu, A.; Chu, D.; Yi, J. Thermostable 1T-MoS₂ Nanosheets Achieved by Spontaneous Intercalation of Cu Single Atoms at Room Temperature and Their Enhanced HER Performance. *Small Struct.* **2023**, *4*, 2300010.
- (36) Kan, M.; Wang, J. Y.; Li, X. W.; Zhang, S. H.; Li, Y. W.; Kawazoe, Y.; Sun, Q.; Jena, P. Structures and Phase Transition of a MoS₂ Monolayer. *J. Phys. Chem. C* **2014**, *118*, 1515–1522.
- (37) Huang, H. H.; Fan, X.; Singh, D. J.; Zheng, W. T. First principles study on 2H–1T' transition in MoS₂ with copper. *Phys. Chem. Chem. Phys.* **2018**, *20*, 26986–26994.
- (38) Zhuang, H. L.; Johannes, M. D.; Singh, A. K.; Hennig, R. G. Doping-controlled phase transitions in single-layer MoS₂. *Phys. Rev. B* **2017**, *96*, 165305.
- (39) Chen, K.; Deng, J.; Shi, Q.; Ding, X.; Sun, J.; Yang, S.; Liu, J. Z. Charge doping induced reversible multistep structural phase transitions and electromechanical actuation in two-dimensional 1T'-MoS₂. *Nanoscale* **2020**, *12*, 12541–12550.

- (40) Mine, H.; Kobayashi, A.; Nakamura, T.; Inoue, T.; Pakdel, S.; Marian, D.; Gonzalez-Marin, E.; Maruyama, S.; Katsumoto, S.; Fortunelli, A.; Palacios, J. J.; Haruyama, J. Laser-Beam-Patterned Topological Insulating States on Thin Semiconducting MoS₂. *Phys. Rev. Lett.* **2019**, *123*, 146803.
- (41) Song, S.; Keum, D. H.; Cho, S.; Perello, D.; Kim, Y.; Lee, Y. H. Room Temperature Semiconductor-Metal Transition of MoTe₂ Thin Films Engineered by Strain. *Nano Lett.* **2016**, *16*, 188–193.
- (42) Guerrero, E.; Karkee, R.; Strubbe, D. A. Phase stability and Raman/IR signatures of Ni-doped MoS₂ from DFT studies. *J. Phys. Chem. C* **2021**, *125*, 13401–13412.
- (43) Li, Q.; Yao, Z.; Wu, J.; Mitra, S.; Hao, S.; Sahu, T. S.; Li, Y.; Wolverton, C.; Dravid, V. P. Intermediate phases in sodium intercalation into MoS₂ nanosheets and their implications for sodium-ion batteries. *Nano Energy* **2017**, *38*, 342–349.
- (44) Wang, M.; Williams, D.; Lahti, G.; Teshima, S.; Aguilar, D. D.; Perry, R.; Koski, K. J. Chemical intercalation of heavy metal, semimetal, and semiconductor atoms into 2D layered chalcogenides. *2D Mater.* **2018**, *5*, 045005.
- (45) Hao, Y.; Wang, Y. T.; Xu, L. C.; Yang, Z.; Liu, R. P.; Li, X. Y. 1T-MoS₂ monolayer doped with isolated Ni atoms as highly active hydrogen evolution catalysts: A density functional study. *Appl. Surf. Sci.* **2019**, *469*, 292 – 297.
- (46) Kondekar, N.; Boebinger, M. G.; Tian, M.; Kirmani, M. H.; McDowell, M. T. The Effect of Nickel on MoS₂ Growth Revealed with *in situ* Transmission Electron Microscopy. *ACS Nano* **2019**, *13*, 7117–7126.
- (47) Mosconi, D.; Till, P.; Calvillo, L.; Kosmala, T.; Garoli, D.; Debellis, D.; Martucci, A.; Agnoli, S.; Granozzi, G. Effect of Ni Doping on the MoS₂ Structure and Its Hydrogen Evolution Activity in Acid and Alkaline Electrolytes. *Surfaces* **2019**, *2*, 531–545.

- (48) Liu, G.; Robertson, A. W.; Li, M. M.-J.; Kuo, W. C. H.; Darby, M. T.; Muhieddine, M. H.; Lin, Y.-C.; Suenaga, K.; Stamatakis, M.; Warner, J. H.; Tsang, S. C. E. MoS₂ monolayer catalyst doped with isolated Co atoms for the hydrodeoxygenation reaction. *Nat. Chem.* **2017**, *9*, 810–816.
- (49) Thomas, J. C.; Chen, W.; Xiong, Y.; Barker, B. A.; Zhou, J.; Chen, W.; Rossi, A.; Kelly, N.; Yu, Z.; Zhou, D.; Kumari, S.; Barnard, E. S.; Robinson, J. A.; Terrones, M.; Schwartzberg, A.; Ogletree, D. F.; Rotenberg, E.; Noack, M. M.; Griffin, S.; Raja, A.; Strubbe, D. A.; Rignanese, G.-M.; Weber-Bargioni, A.; Hautier, G. A substitutional quantum defect in WS₂ discovered by high-throughput computational screening and fabricated by site-selective STM manipulation. *arXiv:2309.08032* **2023**,
- (50) Liu, L.; Wu, J.; Wu, L.; Ye, M.; Liu, X.; Wang, Q.; Hou, S.; Lu, P.; Sun, L.; Zheng, J.; Xing, L.; Gu, L.; Jiang, X.; Xie, L.; Jiao, L. Phase-selective synthesis of 1T' MoS₂ monolayers and heterophase bilayers. *Nat. Mater.* **2018**, *17*, 1108–1114.
- (51) Chen, H.; Chen, Z.; Ge, B.; Chi, Z.; Chen, H.; Wu, H.; Cao, C.; Duan, X. General Strategy for Two-Dimensional Transition Metal Dichalcogenides by Ion Exchange. *Chem. Mater.* **2017**, *29*, 10019–10026.
- (52) Li, J.; Qi, W.; Li, Y. Facial Synthesis of 1T Phase MoS₂ Nanoflowers via Anion Exchange Method for Efficient Hydrogen Evolution. *ChemistrySelect* **2019**, *4*, 2070–2074.
- (53) Chae, S.; Chae, S. S.; Choi, M.; Park, H. M.; Chang, H.; Lee, J.-O.; Il Lee, T. Blocking of the 1T-to-2H phase transformation of chemically exfoliated transition metal disulfides by using a “lattice lock”. *Nano Energy* **2019**, *56*, 65–73.
- (54) Kapuria, N.; Patil, N. N.; Sankaran, A.; Laffir, F.; Geaney, H.; Magner, E.; Scanlon, M.; Ryan, K. M.; Singh, S. Engineering polymorphs in colloidal metal dichalcogenides: precursor-mediated phase control, molecular insights into crystallisation kinetics and promising electrochemical activity. *J. Mater. Chem. A* **2023**, *11*, 11341–11353.

- (55) Dudarev, S. L.; Botton, G. A.; Savrasov, S. Y.; Humphreys, C. J.; Sutton, A. P. Electron-energy-loss spectra and the structural stability of nickel oxide: An LSDA+U study. *Phys. Rev. B* **1998**, *57*, 1505–1509.
- (56) Ernzerhof, M.; Scuseria, G. E. Assessment of the Perdew–Burke–Ernzerhof exchange–correlation functional. *J. Chem. Phys.* **1999**, *110*, 5029–5036.
- (57) Adamo, C.; Barone, V. Toward reliable density functional methods without adjustable parameters: The PBE0 model. *J. Chem. Phys.* **1999**, *110*, 6158–6170.
- (58) Cordero, B.; Gómez, V.; Platero-Prats, A. E.; Revés, M.; Echeverría, J.; Cremades, E.; Barragán, F.; Alvarez, S. Covalent radii revisited. *Dalton Trans.* **2008**, *21*, 2832–2838.
- (59) Choi, J.-H.; Jhi, S.-H. Origin of robust out-of-plane ferroelectricity in d1T-MoS₂ monolayer. *J. Phys.: Condens. Matter* **2019**, *32*, 045702.
- (60) Zhuang, H. Department of Mechanical and Aerospace Engineering, Arizona State University, Tempe, AZ. Personal communication. **May 2022**,
- (61) Pizzochero, M.; Yazyev, O. V. Point defects in the 1T' and 2H phases of single-layer MoS₂: A comparative first-principles study. *Phys. Rev. B* **2017**, *96*, 245402.
- (62) Pallikara, I.; Kayastha, P.; Skelton, J. M.; Whalley, L. D. The physical significance of imaginary phonon modes in crystals. *Electron. Struct.* **2022**, *4*, 033002.
- (63) Croy, A. Bending rigidities and universality of flexural modes in 2D crystals. *J. Phys. Mater.* **2020**, *3*, 02LT03.
- (64) Hu, T.; Li, R.; Dong, J. A new (2×1) dimerized structure of monolayer 1T-molybdenum disulfide, studied from first principles calculations. *J. Chem. Phys.* **2013**, *139*, 174702.
- (65) Komsa, H.-P.; Krasheninnikov, A. V. Native defects in bulk and monolayer MoS₂ from first principles. *Phys. Rev. B* **2015**, *91*, 125304.

- (66) Coutinho, S.; Tavares, M.; Barboza, C.; Frazão, N.; Moreira, E.; Azevedo, D. L. 3R and 2H polytypes of MoS₂: DFT and DFPT calculations of structural, optoelectronic, vibrational and thermodynamic properties. *J. Phys. Chem. Solids* **2017**, *111*, 25 – 33.
- (67) Gresch, D.; Autès, G.; Yazyev, O. V.; Troyer, M.; Vanderbilt, D.; Bernevig, B. A.; Soluyanov, A. A. Z2Pack: Numerical implementation of hybrid Wannier centers for identifying topological materials. *Phys. Rev. B* **2017**, *95*, 075146.
- (68) Soluyanov, A. A.; Vanderbilt, D. Computing topological invariants without inversion symmetry. *Phys. Rev. B* **2011**, *83*, 235401.
- (69) Tang, Q.; Jiang, D. Stabilization and Band-Gap Tuning of the 1T-MoS₂ Monolayer by Covalent Functionalization. *Chem. Mater.* **2015**, *27*, 3743–3748.
- (70) Dhakal, K. P.; Kim, H.; Lee, S.; Kim, Y.; Lee, J.; Ahn, J.-H. Probing the upper band gap of atomic rhenium disulfide layers. *Light Sci. Appl.* **2018**, *7*, 98.
- (71) Schlüter, M. A Pseudopotential Approach to the Electronic Structure of III-IV Layer-Compounds. *J. Phys. Colloques* **1972**, *33*, C3–273–C3–276.
- (72) Li, J.; Han, X.; Li, J.; Zhao, Y.; Fan, C. Structural, electronic and optical properties of famatinite and enargite Cu₃SbS₄ under pressure: A theoretical investigation. *phys. stat. sol. (b)* **2017**, *254*, 1600608.
- (73) Mu, H.-Y.; Yao, Y.-T.; Li, J.-R.; Liu, G.-C.; He, C.; Sun, Y.-J.; Yang, G.; An, X.-T.; Zhang, Y.; Liu, J.-J. Valley Polarization and Valleyresistance in a Monolayer Transition Metal Dichalcogenide Superlattice. *J. Phys. Chem. Lett.* **2020**, *11*, 3882–3888.
- (74) Pasquier, D.; Yazyev, O. V. Unified picture of lattice instabilities in metallic transition metal dichalcogenides. *Phys. Rev. B* **2019**, *100*, 201103.
- (75) Luque, A.; Martí, A.; Stanley, C. Understanding intermediate-band solar cells. *Nat. Photonics* **2012**, *6*, 146–152.

- (76) Yu, K. M.; Walukiewicz, W.; Wu, J.; Shan, W.; Beeman, J. W.; Scarpulla, M. A.; Dubon, O. D.; Becla, P. Diluted II-VI Oxide Semiconductors with Multiple Band Gaps. *Phys. Rev. Lett.* **2003**, *91*, 246403.
- (77) Carter, E. A.; Alidoust, N.; Lessio, M. Multiple band gap Co-Ni oxide compositions and applications thereof. **2019**, patent number:10,256,361.
- (78) Luque, A.; Martí, A. A Metallic Intermediate Band High Efficiency Solar Cell. *Prog. Photovolt: Res. Appl.* **2001**, *9*, 73–86.
- (79) Brunin, G.; Ricci, F.; Ha, V.-A.; Rignanese, G.-M.; Hautier, G. Transparent conducting materials discovery using high-throughput computing. *npj Comput. Mater.* **2019**, *5*, 63.
- (80) Beckman, S. P.; Wang, X.; Rabe, K. M.; Vanderbilt, D. Ideal barriers to polarization reversal and domain-wall motion in strained ferroelectric thin films. *Phys. Rev. B* **2009**, *79*, 144124.
- (81) Wu, M.; Yao, X.; Hao, Y.; Dong, H.; Cheng, Y.; Liu, H.; Lu, F.; Wang, W.; Cho, K.; Wang, W.-H. Electronic structures, magnetic properties and band alignments of 3d transition metal atoms doped monolayer MoS₂. *Phys. Lett. A* **2018**, *382*, 111–115.
- (82) Zhou, W. X.; Ariando, A. Review on ferroelectric/polar metals. *Jpn. J. Appl. Phys.* **2020**, *59*, SI0802.
- (83) Zhang, X.; von Molnár, S.; Fisk, Z.; Xiong, P. Spin-Dependent Electronic States of the Ferromagnetic Semimetal EuB₆. *Phys. Rev. Lett.* **2008**, *100*, 167001.
- (84) Tang, P.; Zhou, Q.; Xu, G.; Zhang, S.-C. Dirac fermions in an antiferromagnetic semimetal. *Nat. Phys.* **2016**, *12*, 1100–1104.
- (85) Gao, Y.; Gao, M.; Lu, Y. Two-dimensional multiferroics. *Nanoscale* **2021**, *13*, 19324–19340.

- (86) Lyu, H.-Y.; Zhang, Z.; You, J.-Y.; Yan, Q.-B.; Su, G. Two-Dimensional Intercalating Multiferroics with Strong Magnetoelectric Coupling. *J. Phys. Chem. Lett.* **2022**, *13*, 11405–11412.
- (87) Nordlander, J.; Campanini, M.; Rossell, M. D.; Erni, R.; Meier, Q. N.; Cano, A.; Spaldin, N. A.; Fiebig, M.; Trassin, M. The ultrathin limit of improper ferroelectricity. *Nat. Commun.* **2019**, *10*, 5591.
- (88) Sui, F.; Jin, M.; Zhang, Y.; Qi, R.; Wu, Y.-N.; Huang, R.; Yue, F.; Chu, J. Sliding ferroelectricity in van der Waals layered γ -InSe semiconductor. *Nat. Commun.* **2023**, *14*, 36.
- (89) Giannozzi, P.; Andreussi, O.; Brumme, T.; Bunau, O.; Buongiorno Nardelli, M.; Calandra, M.; Car, R.; Cavazzoni, C.; Ceresoli, D.; Cococcioni, M.; Colonna, N.; Carnimeo, I.; Dal Corso, A.; de Gironcoli, S.; Delugas, P.; DiStasio, R. A.; Ferretti, A.; Floris, A.; Fratesi, G.; Fugallo, G.; Gebauer, R.; Gerstmann, U.; Giustino, F.; Gorni, T.; Jia, J.; Kawamura, M.; Ko, H.-Y.; Kokalj, A.; Küçükbenli, E.; Lazzeri, M.; Marsili, M.; Marzari, N.; Mauri, F.; Nguyen, N. L.; Nguyen, H.-V.; Otero-de-la-Roza, A.; Paulatto, L.; Poncé, S.; Rocca, D.; Sabatini, R.; Santra, B.; Schlipf, M.; Seitsonen, A. P.; Smogunov, A.; Timrov, I.; Thonhauser, T.; Umari, P.; Vast, N.; Wu, X.; Baroni, S. Advanced capabilities for materials modelling with Quantum ESPRESSO. *J. Phys.: Condens. Matter* **2017**, *29*, 465901.
- (90) Perdew, J. P.; Burke, K.; Ernzerhof, M. Generalized Gradient Approximation Made Simple. *Phys. Rev. Lett.* **1996**, *77*, 3865–3868.
- (91) Grimme, S. Semiempirical GGA-Type Density Functional Constructed with a Long-Range Dispersion Correction. *J. Comput. Chem.* **2006**, *27*, 1787–1799.
- (92) Bengtsson, L. Dipole correction for surface supercell calculations. *Phys. Rev. B* **1999**, *59*, 12301–12304.

- (93) Resta, R. Macroscopic polarization in crystalline dielectrics: the geometric phase approach. *Rev. Mod. Phys.* **1994**, *66*, 899–915.
- (94) Baroni, S.; de Gironcoli, S.; Dal Corso, A. Phonons and Related Crystal Properties from Density-Functional Perturbation Theory. *Rev. Mod. Phys.* **2001**, *73*, 515–562.